Received: 14 September 2023 | Revised: 18 February 2024 | Accepted: 5 April 2024

DOI: 10.1002/cnm.3825

BASIC RESEARCH

WILEY

Impact of left atrial wall motion assumptions in fluid simulations on proposed predictors of thrombus formation

Henrik A. Kjeldsberg[1] | **Carlos Albors**[2] | **Jordi Mill**[2] | **David Viladés Medel**[3] | **Oscar Camara**[2] | **Joakim Sundnes**[1] | **Kristian Valen-Sendstad**[1]

[1]Department of Computational Physiology, Simula Research Laboratory, Oslo, Norway

[2]Department of Information and Communication Technologies, Universitat Pompeu Fabra, Barcelona, Spain

[3]Cardiology Department, Hospital Santa Creu i Sant Pau, Barcelona, Spain

Correspondence
Kristian Valen-Sendstad, Department of Computational Physiology, Simula Research Laboratory, Oslo, Norway.
Email: kvs@simula.no

Funding information
Research Council of Norway through the PARIS project, Grant/Award Number: 311117; ERACoSysMed, Grant/Award Number: 643271; SimCardioTest project (Digital transformation in Health and Care SC1-DTH-06-2020), Grant/Award Number: 101016496; Saga cluster, with resources provided by UNINETT Sigma2 – the National Infrastructure for High Performance Computing and Data Storage, Grant/Award Number: nn9249k

Abstract

Atrial fibrillation (AF) poses a significant risk of stroke due to thrombus formation, which primarily occurs in the left atrial appendage (LAA). Medical image-based computational fluid dynamics (CFD) simulations can provide valuable insight into patient-specific hemodynamics and could potentially enhance personalized assessment of thrombus risk. However, the importance of accurately representing the left atrial (LA) wall dynamics has not been fully resolved. In this study, we compared four modeling scenarios; rigid walls, a generic wall motion based on a reference motion, a semi-generic wall motion based on patient-specific motion, and patient-specific wall motion based on medical images. We considered a LA geometry acquired from 4D computed tomography during AF, systematically performed convergence tests to assess the numerical accuracy of our solution strategy, and quantified the differences between the four approaches. The results revealed that wall motion had no discernible impact on LA cavity hemodynamics, nor on the markers that indicate thrombus formation. However, the flow patterns within the LAA deviated significantly in the rigid model, indicating that the assumption of rigid walls may lead to errors in the estimated risk factors. In contrast, the generic, semi-generic, and patient-specific cases were qualitatively similar. The results highlight the crucial role of wall motion on hemodynamics and predictors of thrombus formation, and also demonstrate the potential of using a generic motion model as a surrogate for the more complex patient-specific motion. While the present study considered a single case, the employed CFD framework is entirely open-source and designed for adaptability, allowing for integration of additional models and generic motions.

KEYWORDS

atrial fibrillation, boundary conditions, computational fluid dynamics, hemodynamics, left atrium, moving domain, thrombus formation

1 | INTRODUCTION

Atrial fibrillation (AF) is the most prevalent cardiac arrhythmia, and is associated with a five-fold increase in thrombotic stroke risk.[1] AF disrupts the active contraction of the atria and, over time, leads to structural remodeling and enlargement of the left atrium (LA).[2,3] The most common hypothesis for explaining the increased thrombotic risk is that enlargement and loss of contraction lead to more stagnant blood flow, in particular in the left atrial appendage (LAA), where more than 99% of thrombi form.[4] Blood stasis is proposed as one of three main drivers of thrombus formation, the other two being endothelial dysfunction and hypercoagulability, collectively known as Virchow's triad.[5] Rough estimates of blood stasis during AF can be obtained by noninvasive medical imaging, which enables quantification and analysis of the cardiac flow patterns (hemodynamics) at the local level. Both phase contrast magnetic resonance imaging (MRI)[6–8] and echocardiography[9–11] can provide details about LA wall motion and capture local blood flow patterns. However, both techniques are limited in their temporal and spatial resolution and include considerable noise, especially in small, fast-moving structures, such as the LA. For these reasons, computational fluid dynamics (CFDs) has been used to complement the available imaging techniques and provide a more detailed analysis of the blood flow in the LA. CFD has previously been used to study how atrial hemodynamics is impacted by anatomy, such as pulmonary vein (PV) configuration[12–15] and LAA complexity,[16,17] volume,[15] and morphology.[13,18–21] Other studies have investigated functional aspects, such as loss of contraction[19,22–25] and the influence of fibrotic regions,[26] as well as the impact of surgical procedures, including left upper lobectomy[27] and LAA occlusion.[28,29] Finally, a number of studies have been conducted to evaluate the effect of CFD model choices, including laminar and large eddy simulation (LES) modeling,[30] non-Newtonian effects,[31] and inflow boundary conditions.[15,30,32]

Abnormal wall shear stress (WSS) is considered a well-established hemodynamic risk indicator to assess cardiovascular pathologies,[33,34] and numerous LA CFD studies have analyzed shear stress-related forces within the LA and LAA.[23,35,36] Various WSS-derived indices have been proposed, and previous research efforts in LA CFD have investigated the correlation of these indices with flow stasis and thrombus formation.[26,37,38] Furthermore, the kinetic energy of blood flow has been frequently computed and considered a potential biomarker for thrombus formation risk,[27,39,40] also measurable through and comparable with noninvasive medical imaging techniques[41] for validation.

Although previous research efforts have provided considerable insight into atrial hemodynamics and potential biomarkers for thrombus formation, there are still considerable knowledge gaps. In particular, there is a lack of knowledge on how CFD modeling assumptions impact hemodynamic indices and other flow-related quantities.[32,42] For example, many studies model the LA wall as rigid,[32] which would be a severe simplification for a healthy LA, where volume varies considerably throughout the cardiac cycle.[43,44] However, it may be a reasonable approximation in fibrillating LA, when function is heavily reduced and the chamber is enlarged, severely reducing the change in relative volume.[44,45] A few studies have considered the differences in local hemodynamics and predictors of thrombus formation between rigid and moving wall simulations,[30,40] but none of these include a comprehensive and quantitative analysis of the errors that arise from this modeling assumption. Furthermore, of the existing moving wall simulations in the literature, many use simplified[14,26,46] or random high frequency[20,47] wall motions. Some previous works also consider fluid–structure interaction (FSI)-based approaches.[39,48,49] However, these are computationally demanding, and necessitate additional patient-specific measurements, such as personalized material properties.

In the present study, we aimed to investigate the impact of rigid versus dynamic wall modeling assumptions on local hemodynamics and in-silico hemodynamic indices of thrombogenic risk in the main LA cavity and the LAA. In addition, we sought to evaluate whether generic motion models could serve as a viable surrogate for patient-specific data. Our analysis compared rigid wall simulations with two synthetic generic motions and one patient-derived motion from 4D CT images, focusing on their effects on flow dynamics, WSS-derived indices, and kinetic energy.

2 | METHOD

2.1 | Patient data

We considered one LA geometry of a patient with permanent AF, acquired from cardiac-gated time-resolved (4D) CT, and provided by Hospital de la Santa Creu i Sant Pau, Barcelona, Spain. Medical images were acquired with a Somatom Force CT scanner (Siemens Healthineers, Erlangen, Germany), producing DICOM files with pixel dimensions of 0.41 mm in the x–y plane and 0.90 mm in the z-direction, acquired every 5% of the cardiac cycle, from 0 to 95% of the

R–R interval, resulting in 20 images. The image acquisition was approved by the institutional Ethics Committee and the patient gave informed consent.

2.2 | Image segmentation and registration

The DICOM image representing 0% of the RR-interval, corresponding to the onset of atrial diastole, was segmented using the semi-automatic tools available in *Slicer*[51] using a seed-growing technique. The resulting segmentation mask is shown in Figure 1A. This segmentation mask was then minimally smoothed and clipped at the boundaries using MeshMixer,[52] resulting in the 3D reference surface model shown in Figure 1B, where the colors highlight the LAA, the five PV inlets, and the mitral valve (MV) orifice in red, blue, and yellow, respectively.

To obtain the patient-specific LA wall motion, the remaining 19 medical images underwent image registration against the reference image (captured at 0% RR) using the *Advanced Normalization Tools* software.[50] This image registration yielded 19 three-dimensional displacement fields, each representing LA wall motion throughout a cardiac cycle. These fields were then mapped onto the 3D reference surface model, producing 19 unique surface models that describe the LA's displacement over time. A selection of these models is displayed in Figure 1C. Although in the present study we only considered the LA, the left ventricle was also segmented and registered in order to compute its volume change through the cardiac cycle, which provided the outflow boundary condition for the LA flow simulations.

2.3 | Mesh generation

We used the fully automated preprocessing tools of *VaMPy*,[53] adapted to handle moving domains, to generate the volumetric mesh. Cylindrical flow extensions were added at the PV boundaries prior to meshing to accurately represent the circular Womersley profile and to ensure fully developed inflow. The motion of the PV boundaries near the LA cavity was relatively small, measuring less than one fifth of the local radius, and we concluded that flow extensions with a length of two times the local radius was sufficient to capture the motion and minimally affect the flow. The image-based motion of the original inlet and outlet boundaries was preserved and then reduced linearly toward the fixed ends of the flow extensions. A similar flow extension, with length two times the local radius, was added at the MV orifice. The resulting mesh is shown in Figure 2A, consisting of 3.5 million tetrahedral elements, including LAA refinement. The average cell length was $\Delta x = 0.9$ and 0.3 mm in the LA and LAA, respectively. Four boundary layers, visible in the zoomed-in cross section of the LAA in Figure 2B, were added to further resolve the spatial fluid gradients near the wall, which were used to compute the hemodynamic indices of interest.

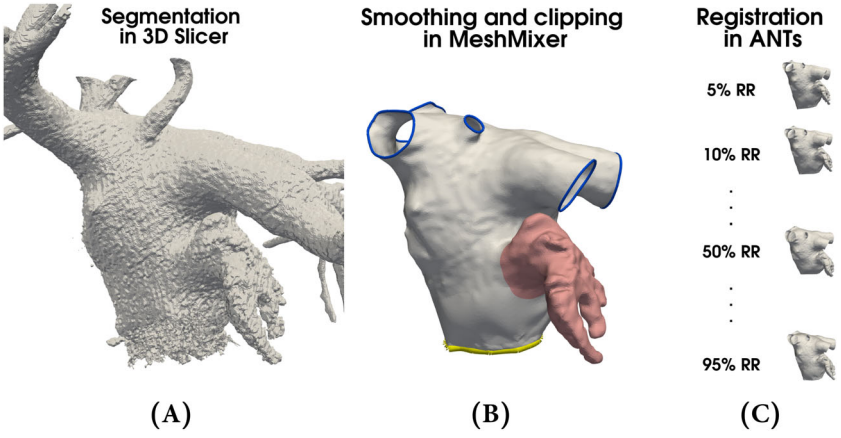

FIGURE 1 In (A), the segmentation mask of the patient-specific left atrium at the start of atrial diastole. In (B), the smoothed 3D model of the atrium, highlighting the left atrial appendage in red, the pulmonary vein inlets in blue, and the mitral valve orifice in yellow. In (C), a subset of the displaced LA surface models from the image registration process, from 5% to 95% of the RR-interval using the *Advanced Normalization Tools* software.[50]

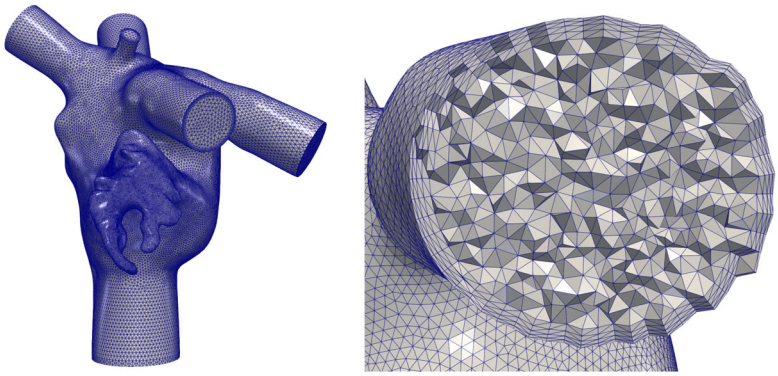

FIGURE 2 In (A), the volumetric mesh of the left atrium, including the refined region near the appendage, and cylindrical flow extensions at the pulmonary vein boundaries and mitral valve orifice. In (B), a zoomed-in view of the left atrial appendage, showing the refined elements in this region, and the four boundary layers present throughout the volumetric mesh.

2.4 | Wall boundary conditions

The main purpose of this study was to assess the impact of rigid versus moving wall boundary conditions in the LA-based fluid simulations. As noted above, we considered three different wall boundary conditions, all described by the function $\boldsymbol{g}(\boldsymbol{x},t) \in \mathbb{R}^3$, which represents the LA wall motion, where $\boldsymbol{x}$ and t denote the spatial coordinates and time, respectively. The following three LA wall motion behaviors were considered:

1. An assumption of rigid walls, with $\boldsymbol{g}(\boldsymbol{x},t) = 0$.
2. A generic moving boundary condition, previously proposed by Corti et al.,[36] where the LA wall motion was described through a separation of the temporal and spatial variation:

$$\boldsymbol{g}(\boldsymbol{x},t) = \boldsymbol{F}(\boldsymbol{x})h(t). \tag{1}$$

In order to precisely control the magnitude of LAA deformation, the spatial component $\boldsymbol{F}(\boldsymbol{x})$ was decomposed into two separate terms, describing, respectively, the motion of the LA cavity and the LAA:

$$\boldsymbol{F}(\boldsymbol{x}) = \boldsymbol{f}_{\mathrm{LA}}(\boldsymbol{x}) + k\boldsymbol{f}_{\mathrm{LAA}}(\boldsymbol{x}). \tag{2}$$

Here, k is a constant, which was calibrated to align the contraction of the LAA with the patient-specific displacement data. In this way, the change in LA and LAA volume could be altered independently of each other. In instances where patient-specific data are unavailable, the parameter k can be calibrated based on clinical measurements of LAA contraction.[54] The space-dependent functions $\boldsymbol{f}_{\mathrm{LA}}(\boldsymbol{x})$ and $\boldsymbol{f}_{\mathrm{LAA}}(\boldsymbol{x})$ were defined as:

$$\boldsymbol{f}_{[\mathrm{LA,LAA}]}(\boldsymbol{x}) = \frac{\varphi(\boldsymbol{x})}{\max(\varphi(\boldsymbol{x}), 1-\varphi(\boldsymbol{x}))}\left(\boldsymbol{x} - \boldsymbol{x}_G^{[\mathrm{LA,LAA}]}\right), \tag{3}$$

where $\boldsymbol{x}_G^{[\mathrm{LA,LAA}]}$ is the center of mass of the LA or LAA. Note that we adjusted the definition of Equation (3) from the paper by Corti et al. to incorporate the longitudinal motion present at the MV orifice,[55,56] while maintaining the PVs in a fixed position. The function φ is the solution of the following Laplace–Beltrami problem[57]:

$$-\Delta\varphi = 0 \quad \text{in } \partial\Omega, \tag{4}$$

$$\varphi = 0 \quad \text{on } \Gamma^{\mathrm{PV}^i}, \tag{5}$$

$$\varphi = 1 \quad \text{on } \Gamma^{\text{MV}}, \tag{6}$$

where $\partial\Omega$ denotes the domain boundary, Γ^{PV^i} are the PV boundaries, and Γ^{MV} is the MV orifice boundary.

The temporal component $h(t)$ is derived from the rate of change of the time-varying LA volume, and directly influences the magnitude of wall displacement. $h(t)$ was constructed by applying the Reynolds transport theorem[58] to Equation (1) and solving for $h(t)$, to give:

$$h(t) = \left[\int_{\partial\Omega} \boldsymbol{F} \cdot \boldsymbol{n} \, \mathrm{d}S \right]^{-1} \frac{\mathrm{d}V_{\text{LA}}(t)}{\mathrm{d}t}. \tag{7}$$

Here, $\partial\Omega$ denotes the domain boundary, $\boldsymbol{n}$ is the surface normal vector, and $\mathrm{d}V_{\text{LA}}/\mathrm{d}t$ is the rate of change in LA volume. We considered two scenarios; one where the temporal volume change was based on a generic LA volume curve obtained from the existing literature,[59] and one where this specific rate of change was obtained from the time-resolved CT images.

3. A patient-specific LA wall motion obtained from the image registration of the time-resolved CT images. The motion of the LA endocardium was imposed at each time step using the time-resolved CT image data. The endocardium displacement for each vertex in the 3D model was approximated using a third-order spline with periodic boundary conditions, ensuring continuous coverage of a full cardiac cycle. The endocardium velocity $\boldsymbol{g}(\boldsymbol{x}, t)$ was then computed as the first-order derivative of the resulting spline and prescribed as the wall boundary condition.

In the following, we will refer to these three wall boundary conditions as the rigid, generic, and patient-specific model, respectively. Regarding the two scenarios based on the generic model, we will refer to the one employing a generic LA volume curve as the generic case, and the one utilizing a patient-derived LA volume curve as the semi-generic case. A comparison of the displacement between the generic, semi-generic, and patient-specific cases is presented in Figure 3. The displacement field is represented by vectors, scaled by the displacement magnitude. Distinctly, the generic and semi-generic cases exhibit a uniform pattern, while the patient-specific case displays highly individualized displacement, with diverse vector orientations and magnitude.

The two moving wall conditions also required calculating the motion of the internal nodes in the volumetric mesh, which we defined as a harmonic extension of the endocardium velocity, obtained by solving:

$$\nabla \cdot (\alpha(\boldsymbol{x}) \nabla \boldsymbol{w}) = 0 \quad \text{in} \Omega, \tag{8}$$

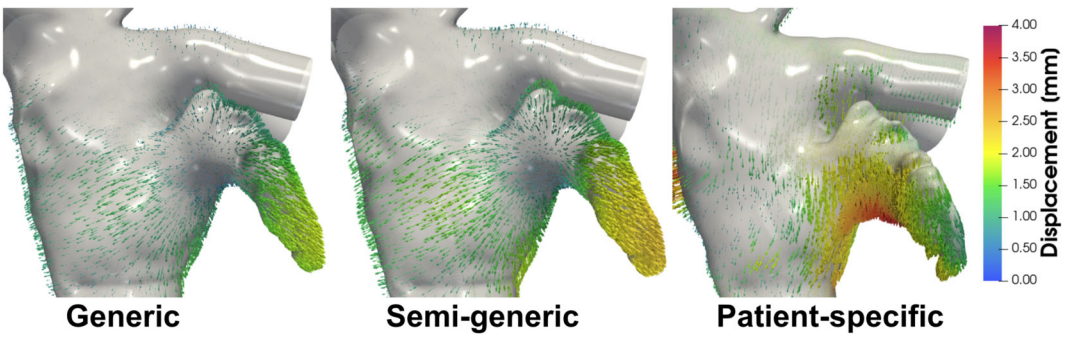

FIGURE 3 A comparative visualization snapshot of the displacement fields for the three distinct motion scenarios—generic, semi-generic, and patient-specific—taken at the onset of atrial systole. The fields are represented by vectors representing the magnitude and direction of displacement, and are colorized by the displacement magnitude. In the generic and semi-generic cases, displacement direction mainly points uniformly away from the appendage's center of mass. In contrast, there is a more pronounced longitudinal displacement acting on the appendage in the patient-specific case.

$$\boldsymbol{w} = \boldsymbol{g} \quad \text{on} \partial\Omega. \tag{9}$$

Here, $\boldsymbol{w} = \boldsymbol{w}(\boldsymbol{x}, t)$ represents the mesh velocity in the 3D domain Ω, $\boldsymbol{g} = \boldsymbol{g}(\boldsymbol{x}, t)$ describes the endocardium velocity on the boundary $\partial\Omega$, and α is a variable diffusion parameter, set to depend on the finite element cell volume.[60] To determine whether remeshing was required, we computed the determinant (J) of the local deformation gradient tensor, which is an indicator of volume change. In the three moving cases, we found that $0.98 < J < 1.03$ for all elements, which indicated minimal volume change and relatively small deformation gradient, and therefore geometrical remeshing was not necessary.

2.5 | Inflow- and outflow boundary conditions

A Womersley flow profile was prescribed at the PVs, with the target inlet velocity at each PV defined as the ratio between the instantaneous flow rate through each PV and its respective cross-sectional area. The geometry and flow distribution is shown in Figure 4A. The individual PV flows Q^i_{PV} were calculated by dividing the total Q_{PV} according to the cross-sectional areas of the PVs, since patient-specific measurements of individual PV flow rates were not available. The total flow PV flow was determined from the measured mitral flow and conservation of mass:

$$Q_{\text{PV}} + Q_{\text{MV}} + \frac{\mathrm{d}V_{\text{LA}}(t)}{\mathrm{d}t} = 0. \tag{10}$$

Here, Q_{MV} represents the flow through the MV orifice. For the generic case, Q_{MV} was based upon a representative AF waveform from the literature.[19] In contrast, for the semi-generic and patient-specific cases, Q_{MV} was determined from the left ventricle volume curve, which was derived from the dynamic medical images. Meanwhile, V_{LA} denotes the time-dependent LA volume, shown for the four scenarios in the upper panel of Figure 4B.

The lower panel of Figure 4B shows the total PV flow calculated as the sum of MV flow and atrial volume change. During atrial diastole the MV is closed, which gives $Q_{\text{PV}} = 0 = \mathrm{d}V_{\text{LA}}/\mathrm{d}t$ in this phase, and consequently $Q_{\text{PV}} = 0$ for the rigid case, as seen in the left part of the lower panel of Figure 4B. For the outflow boundary at the MV, we applied a zero-pressure boundary condition.

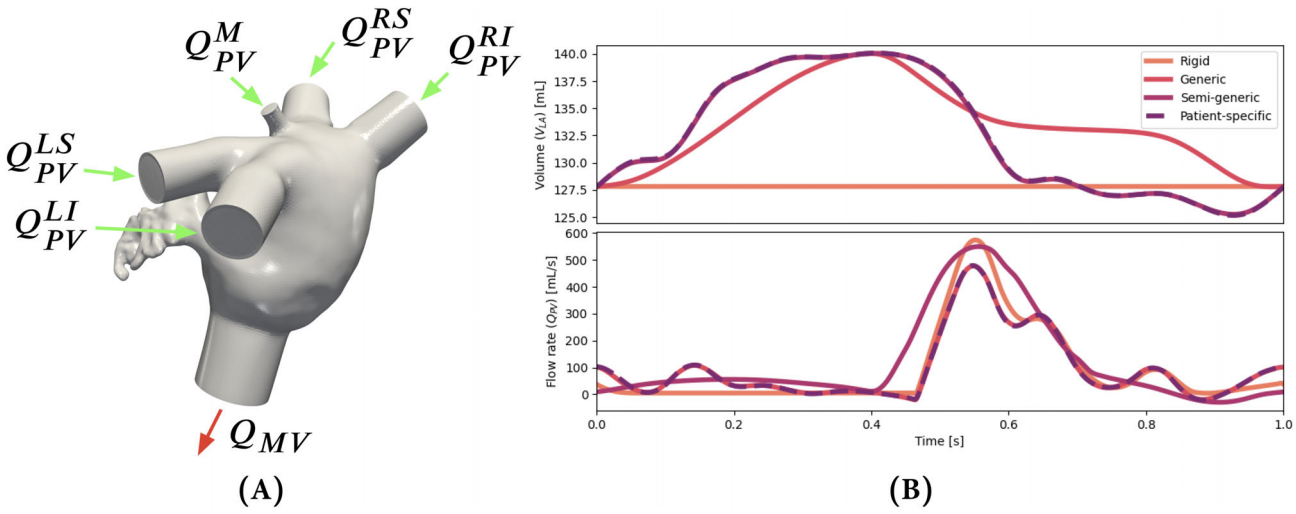

FIGURE 4 In (A), left atrial geometry and flow distribution. The total flow rate Q_{PV} is split between the five pulmonary veins: middle (M), right superior (RS), right inferior (RI), left superior (LS), and left inferior (LI). Q_{MV} is the outflow through the mitral valve orifice. In the upper and lower row of (B), we show the change in atrial volume over one cardiac cycle for the different boundary conditions, and the corresponding total pulmonary vein flow rates, respectively.

2.6 | CFDs simulations

We used the open-source CFD solver *OasisMove* for fluid simulations, which handles moving domains by expressing the Navier–Stokes equations in the arbitrary Lagrangian–Eulerian (ALE) formulation. The solver was previously verified and validated by comparing it with unstable cardiovascular flow in high-resolution simulations and laboratory experiments in a left ventricle model.[61] *OasisMove* is an extension of the solver *Oasis*,[62] which has been validated[63,64] and widely used for hemodynamic simulations.[65–69]

We used a space/time centered incremental pressure correction scheme, with first-order Lagrange finite elements ($\mathbb{P}_1$) for spatial discretization of velocity and pressure, which is second-order accurate in the L_2 norm.[61] By using an Adams–Bashforth-projected convective term and a Crank–Nicholson discretization of the convected velocity, we ensure a second-order accuracy in time, while minimizing numerical dispersion and diffusion errors.[70] Blood was modeled as an incompressible Newtonian fluid with a density of $\rho = 1060$ kg/m^3 and dynamic viscosity of $\mu = 0.0035$ Pa·s. To address the presence of local negative velocity components at the outflow, we imposed backflow stabilization at the MV orifice with minimal impact on the upstream flow,[71] as previously applied in LA simulations.[42,46,72] A summary of parameters related to the CFD model and the simulation setup is provided in Table 1.

2.7 | Hemodynamic indices and kinetic energy analysis

As noted above, abnormal WSS is a well-established hemodynamic risk indicator,[33,34] and several WSS-derived indices have been proposed and associated with flow stasis and thrombus formation.[26,37] The WSS represents the mechanobiological effect of shear stress on the endocardium, where low values correspond to low flow velocity, which is associated with increased risk of thrombus formation in the LAA.[73] The WSS-derived indices considered here include the oscillatory shear index (OSI), relative residence time (RRT), and endothelial cell activation potential (ECAP),[74–76] see Table 2 for the definitions. All the indices considered here are time-averaged quantities, estimated over a single or multiple cardiac cycles. The OSI is a nondimensional parameter that captures the flow oscillation by relating the WSS direction with its magnitude, ranging from 0 for constant flow to 0.5 when the flow direction is entirely reversed. RRT serves as an indicator of blood particle residence time near the LA wall and is related to platelet aggregation in the endothelium.[75,77] Finally, the ECAP index is associated with endothelial susceptibility, which can ultimately increase the risk of thrombus formation,[76] and is calculated as the ratio between OSI and WSS. The computation of ECAP is inconsistent in the literature, and has been defined using an area averaged WSS,[76] by normalization,[26] and by direct computation.[36,78] The latter formulation appears to be the most favored and is the one we consider here, as defined in Table 2.

Furthermore, we investigated the kinetic energy (KE) per unit mass in the LA and LAA, as an indicator of the general properties of the flow field and the energy distribution within the atrium. The mathematical definitions of the

TABLE 1 List of mesh and simulation parameters related to the setup of the main fluid simulations.

Parameter	Value	Unit
Number of cardiac cycles	5	-
Cardiac cycle duration, T	1000	ms
Time step size, Δt	0.2	ms
LA cell size, Δx_{LA}	0.9	mm
LAA cell size, Δx_{LAA}	0.3	mm
Fluid density, ρ	1060	kg/m^3
Dynamic viscosity, μ	0.0035	Pa·s
$\mathrm{CFL}_{\mathrm{max}}$	0.4	-
$\mathrm{CFL}_{\mathrm{mean}}$	0.05	-
Velocity finite element order	$\mathbb{P}_1$	-
Pressure finite element order	$\mathbb{P}_1$	-

Note: We display the mean and maximum (pointwise) Courant–Friedrichs–Lewy (CFL) number observed in the left atrium over one cardiac cycle.

TABLE 2 List of the relevant indicators considered in the present study.

Indicator	Abbreviation	Definition	Unit
Wall shear stress	WSS	$\frac{1}{T}\int_0^T \lvert\tau\rvert \mathrm{d}t$	[Pa]
Oscillatory shear index	OSI	$\frac{1}{2}\left(1-\frac{\left\lvert\int_0^T \tau \mathrm{d}t\right\rvert}{\int_0^T \lvert\tau\rvert \mathrm{d}t}\right)$	[−]
Relative residence time	RRT	$[(1-2\cdot \mathrm{OSI})\cdot \mathrm{WSS}]^{-1}$	[Pa^{-1}]
Endothelial cell activation potential	ECAP	$\frac{\mathrm{OSI}}{\mathrm{WSS}}$	[Pa^{-1}]
Kinetic energy	KE	$\frac{1}{2}(u^2+v^2+w^2)$	[$\mathrm{cm}^2/\mathrm{s}^2$]

Note: Here, τ is the wall shear stress vector, t is the time, T is the length of the cardiac cycle, and u, v, and w are the velocity components.

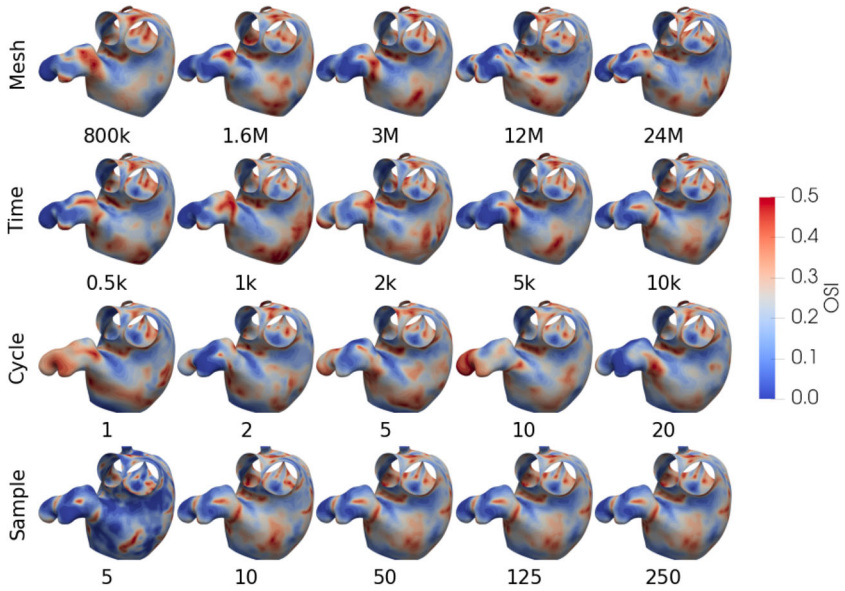

FIGURE 5 A visual subset of the convergence study, displaying the oscillatory shear index in the left atrium, ranging from 0 to 0.5. We present the four separate studies per row, while the values shown below each model represents the amount of tetrahedral cells, number of time steps per cardiac cycle, cycle number, number of data samples for the mesh, time, cycle, and sample convergence study, respectively.

hemodynamic indices and KE are listed in Table 2, and have been computed using the postprocessing tools of the *VaMPy* software.[53] We applied morphological tools implemented in Man*morphMan*[79] to objectively clip and separate the LA and LAA. Subsequently, we individually analyzed these regions for hemodynamic indices and KE.

2.8 | Convergence studies

Four distinct convergence studies were conducted to ensure the robustness and precision of our findings. Specifically, we tested the mesh resolution, time step size, cycle-to-cycle convergence, and data sampling rate, all of which can potentially affect the hemodynamic results. All the convergence studies were performed using rigid wall boundary conditions, in order to reduce the computational load to manageable levels. Furthermore, the geometric complexity of the innermost lobes of the LAA was slightly reduced due to mesh entanglement issues that arose from including the boundary layers. Despite this modification, the general shape and structure of the LAA remain intact, and the impacts of this modification on the results are discussed in Data **S1**. Note that this modification was performed exclusively for the convergence studies. Thus, the main results presented in Section 3 are derived from the original unmodified 3D LA surface model of the LA.

Figure 5 shows a subset of the results, using OSI as a representative example, with values scaled between 0 and 0.5. Each row represents one of the four separate studies, and the values below each model indicate the number of

tetrahedral cells, the number of time steps per cardiac cycle, the cycle number, and the number of data samples, respectively. Results for the remaining indices can be found in Data **S1**. The convergence studies were conducted using a mesh consisting of 3.3 M cells, a time step of $\Delta t = 0.2$ ms, running five cardiac cycles each lasting $T = 1$ s, and storing a total of 250 data points per cycle.

The mesh convergence study was performed using uniformly dense volumetric meshes, ranging between 800 k and 24 M tetrahedral cells, and showed that the OSI values in the cavity varied in location and increased slightly as the mesh was refined. In contrast, OSI in the LAA gradually decreased as the mesh was refined, as depicted in the first row of Figure 5. In particular, the two coarsest meshes (800 k and 1.6 M) exhibit substantial regional differences within the LAA compared with higher resolutions. This convergence study revealed that the LAA necessitated a higher resolution, and was therefore refined for the following studies. Furthermore, the required temporal resolution was assessed by varying the number of time steps per cardiac cycle between 500 and 10,000. These simulations were performed using a mesh consisting of 3.3 M tetrahedral cells, and the results are shown in the second row of Figure 5. Considerable differences in location and magnitude can be observed inside the LAA, in particular for the 2000 time step simulation, which displays large OSI at the apex of the innermost lobe.

Few studies in the LA literature consider cycle-to-cycle differences in LA hemodynamics,[25,31,40] while most maintain that cycle convergence can be achieved within two or three cardiac cycles. We considered simulations over 20 s for our convergence study, using 5000 time steps per cardiac cycle, resulting in a total of 100,000 time steps for a mesh consisting of 3.3 M cells. A subset of the results is presented in the third row of Figure 5, where we observe marginal cycle-to-cycle differences in the LA cavity, and more considerable variability in the LAA. Consequently, we decided to include the four last cardiac cycles in our analysis due to substantial variations in hemodynamics between cycles, particularly within the LAA.

Lastly, we conducted a convergence study for the sampling rate of data for the estimation of hemodynamic quantities per cardiac cycle, also known as phase convergence.[80] Data were sampled over the last cardiac cycle, with sampling rates ranging from 5 to 250 samples per cycle. The results displayed notable qualitative differences with less than 10 samples per cycle, as illustrated in the fourth row of Figure 5. We observed negligible differences beyond 50 samples per cycle, both in the LA cavity and in the LAA. Based on this study, we chose to sample 125 data points per cardiac cycle, as additional samples did not noticeably impact the results.

Further qualitative and quantitative analyses of the four convergence studies can be found in Data **S1**.

3 | RESULTS

Figure 6 shows the hemodynamic indices of interest—WSS, OSI, RRT, and ECAP—for the LA cavity and appendage separately, averaged over the four last cardiac cycles, with appropriately scaled color bars in the LA and LAA. Note that we use logarithmic scales for WSS, RRT, and ECAP, to emphasize the qualitative differences. Furthermore, for the appendage, we have scaled the WSS range down by a factor of a thousand, increased the RRT range by the same factor, and increased the ECAP range hundredfold relative to the hemodynamic indices in the cavity.

Figure 6A presents the hemodynamic indices in the LA cavity, where we observe minimal variance in magnitude across the four scenarios, except for the generic case, which exhibits notably higher WSS. There are also noticeable variations in the region of extreme values. For instance, the area of minimum ECAP, indicated by the black regions on the cavity, presents regional variation, ranging from the vicinity of the left superior PV to the central zone of the cavity. In contrast, Figure 6B, which presents the hemodynamic indices in the LAA, shows considerable differences between the rigid, generic, semi-generic, and patient-specific cases. In the rigid case, the WSS values rapidly diminish toward the inner lobes of the appendage, which are the protruding, rounded parts of the LAA. In contrast, the patient-specific case shows noticeably higher and more uniformly distributed patterns of WSS, with local minima located at the lobes. OSI values are relatively low throughout the rigid case and overall higher in the generic case, while regions of high OSI are prominent and comparable between the semi-generic and patient-specific cases. Furthermore, the rigid case displays areas of high RRT and ECAP in contrast to the generic, semi-generic, and patient-specific cases. However, the both generic cases show noticeable deviations in RRT and ECAP compared with the patient-specific case.

The box plot in Figure 7 shows a quantitative representation of the variability in hemodynamic indices. The left column displays values for the LA cavity, while the right column shows values inside the LAA for the four scenarios. Each row display a key hemodynamic index of interest: WSS, OSI, RRT, and ECAP, using logarithmic scales for the WSS,

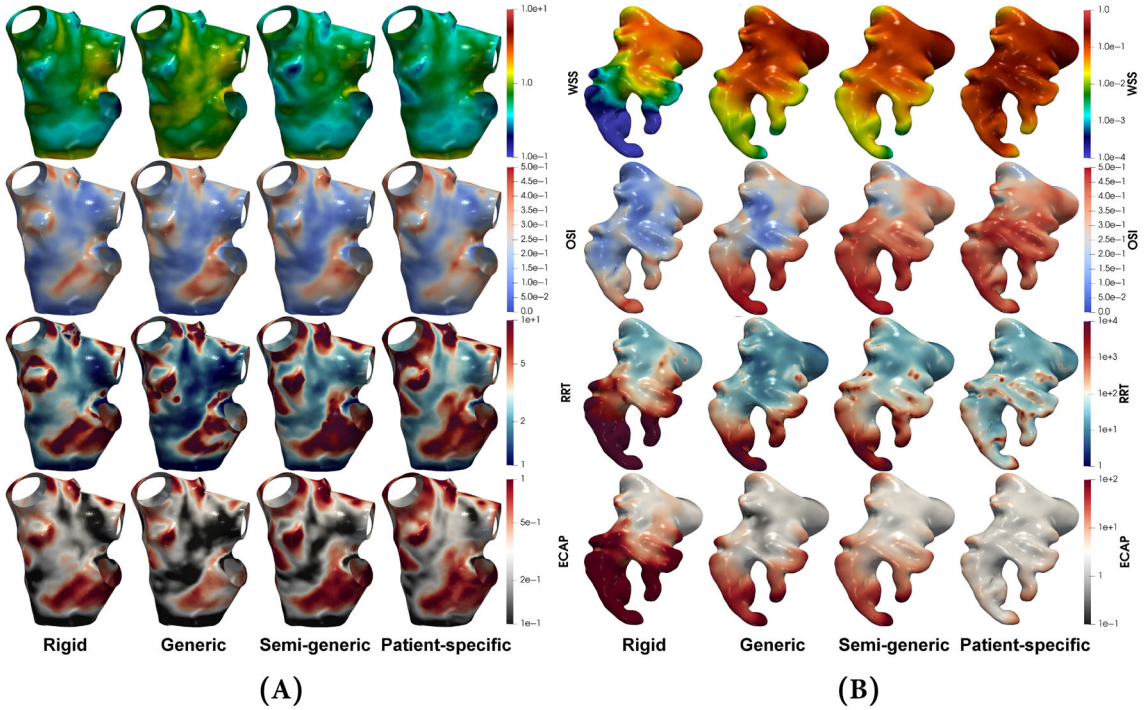

FIGURE 6 In panels (A) and (B), visualizations of key hemodynamic indices—wall shear stress (WSS), oscillatory shear index (OSI), relative residence time (RRT), and endothelial cell activation potential (ECAP)—are presented for the left atrial cavity and appendage, respectively. Note that the WSS, RRT, and ECAP use logarithmic scales.

RRT, and ECAP. We present the box plot for the four last cardiac cycles, where the figure legend represents the cycle number.

The hemodynamic indices in the LA cavity are presented in the left column of Figure 7. The box plots show minor differences in both median and quartile ranges between the rigid, semi-generic, and patient-specific cases, while it is 0.2–0.3 Pa higher in the generic case. Specifically, WSS values are only marginally higher in the rigid case, closer to 0.6 Pa compared with 0.5 Pa in the semi-generic and patient-specific cases, while the generic case displays a median of 0.75 Pa. We observe OSI values around 0.2, while RRT values lie between 2 and 4 Pa^{-1}. Similarly, ECAP values are relatively low in the LA cavity for all scenarios, with median values between 0.27 and 0.45 Pa^{-1}. Furthermore, the box plots reveal a low variation in the magnitude of the hemodynamic index between cardiac cycles, with differences of less than 10% observed for all indices.

Hemodynamic indices in the LAA are presented in the right column of Figure 7. We observe notable differences in all hemodynamic indices between the four scenarios. The median WSS values in the rigid case are comparably low, with high intercycle and regional variability, ranging between 4 and 23 mPa, with the lowest values at the tip of the LAA. In contrast, the WSS is higher, with lower intercycle variability, with median values of 66, 70, and 153 mPa in the generic, semi-generic, and patient-specific cases, respectively. OSI values range between 0.09 and 0.34 in the rigid case, between 0.29 and 0.34 in the generic case, while the semi-generic and patient-specific cases display higher values closer to 0.41. Focusing on RRT, the values are markedly higher compared with those experienced in the LA cavity, with median values ranging between 30 and 700 Pa^{-1}. The rigid case exhibits the highest RRT values, 10, 5, and 9 times higher than the generic, semi-generic, and patient-specific cases, respectively. Similarly, the ECAP values are noticeably higher in the rigid case, ranging between 5 and 70 Pa^{-1}, compared with the median values of 4, 6, and 3 Pa^{-1} in the moving cases. In addition, we observe a larger variability in RRT and ECAP in the two generic cases compared to the patient-specific case.

In Figure 8, we present box plots using logarithmic scale for the KE in the LA and LAA on the left- and right-hand side, respectively, across the four scenarios. The results are presented for the four last cardiac cycles, where the figure legend represents the cycle number. KE display notable differences in the LA among the scenarios, as illustrated on the left-hand side of Figure 8. The median KE values are approximately 100, 160, 70, and 70 cm^2/s^2 for the rigid, generic, semi-generic, and patient-specific cases, respectively. Furthermore, the median KE values display a variation of less

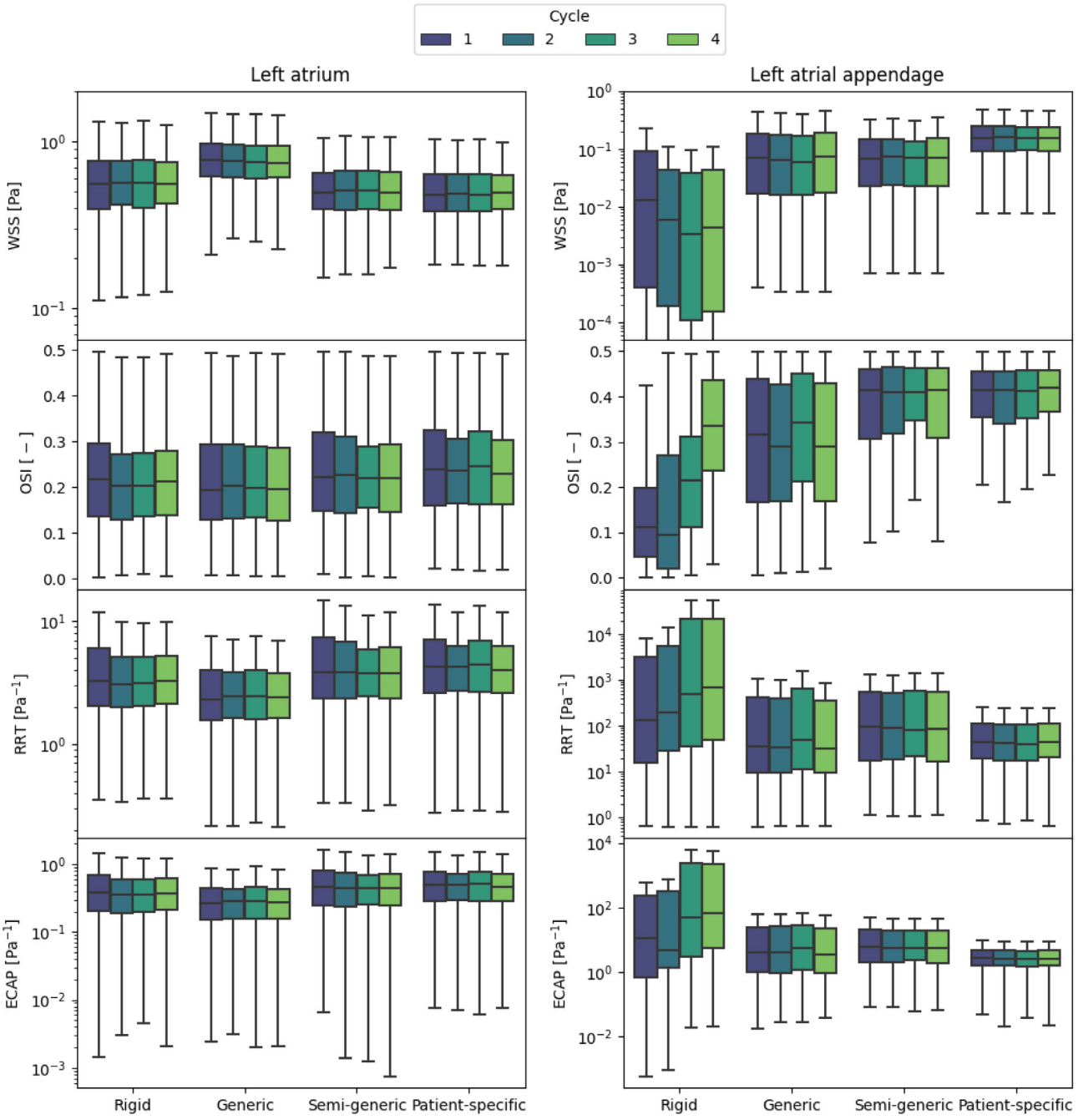

FIGURE 7 A box-plot illustrating the hemodynamic indices quantified over the four last cardiac cycles, as denoted in the figure legend, for the respective wall boundary conditions, with analysis in the atrium cavity and appendage presented in the left and right column, respectively. Note the logarithmic scale used for the wall shear stress (WSS), relative residence time (RRT), and endothelial cell activation potential (ECAP) indices.

than 6% between cycles, and the rigid and generic cases demonstrate higher KE within the cavity compared with the semi-generic and patient-specific cases. Averaging over the cavity, the KE is 1.7, 2.6, 1.3, and 1.3 mJ in the rigid, generic, semi-generic, and patient-specific cases, respectively. On the contrary, the right side of Figure 8 shows considerable differences in KE in the LAA between the scenarios, as well as between cardiac cycles. The patient-specific case demonstrates the highest KE values, with a median value around 5 cm^2/s^2, 40–400 times higher than the rigid case's median value, which ranges from 0.012 to 0.12 cm^2/s^2. The generic case displays a median KE value of 1.7 cm^2/s^2, while the semi-generic case shows slightly higher values at 2.0 cm^2/s^2. Differences in KE between cycles are most pronounced in the rigid case, reaching up to 12-fold differences, with large variability, while the three moving scenarios remain

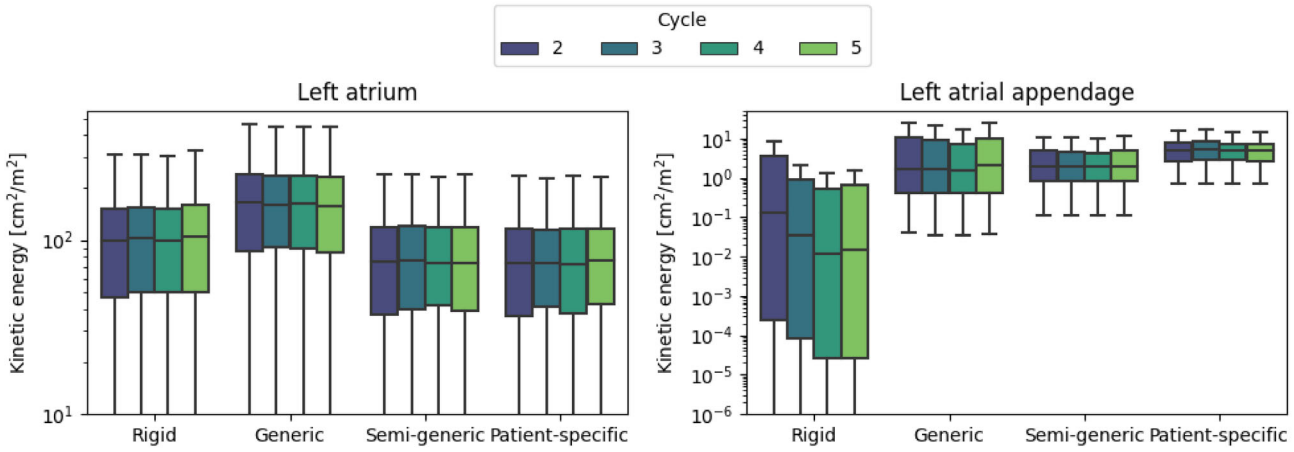

FIGURE 8 A box-plot illustrating the kinetic energy quantified over the four last cardiac cycles, as denoted in the figure legend, for the respective wall boundary conditions, with analysis in the atrium cavity and appendage shown in the left and right column, respectively. Note the logarithmic scale used for the kinetic energy values.

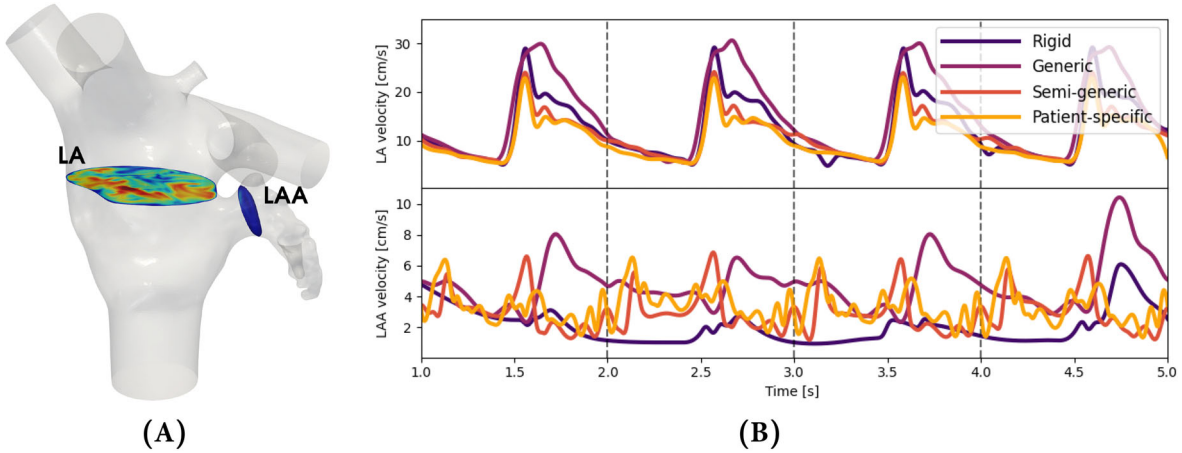

FIGURE 9 In (A), we present cross-sectional slices in the left atrial cavity (LA) and at left atrial appendage (LAA) orifice, colored by the velocity magnitude. In (B), the corresponding mean velocity profiles in magnitude, sampled from the aforementioned cross-sectional slices. The profiles are acquired over the four last cardiac cycles, separated by the dashed line.

below 10% variability. Within the LAA, the average KE is 4.2, 11.2, 4.2, and 5.2 μJ in the rigid, generic, semi-generic, and patient-specific cases, respectively.

Figure 9 shows the mean velocity profiles sampled from two different cross-sectional slices, one in the LA cavity and one in the LAA orifice. The two slices are representatively shown in the rigid case in panel A, while panel B shows the velocity profiles over the four last cardiac cycles, which are separated by the dashed vertical line at 0% of the RR-interval. The upper panel shows the mean flow velocity through the LA cavity slice, which is relatively stable from cycle to cycle and also shows a strong similarity between the rigid, semi-generic, and patient-specific cases. The generic case has a slightly elevated peak velocity, and notably a larger cardiac output. The LAA orifice velocity profiles are shown in the lower panel and show marked differences between the four curves. In the rigid case, we observe a longer period of stagnant flow, with velocities below as 2 cm/s during the second, third, and fourth cardiac cycle. The generic case shows a slightly more variable flow pattern, with heightened flow velocities reaching 10 cm/s in the fourth cardiac cycle. The remaining moving cases display continuous and oscillatory flow behavior, indicating a substantially more active filling and emptying process.

Finally, we present the velocity vector fields represented by line integral convolution through a cross-sectional slice in the LA and LAA in Figure 10, colored by the velocity magnitude. The upper row shows the velocity during atrial diastole, showing complex vortex patterns present in the LA cavity for the four boundary condition scenarios. In

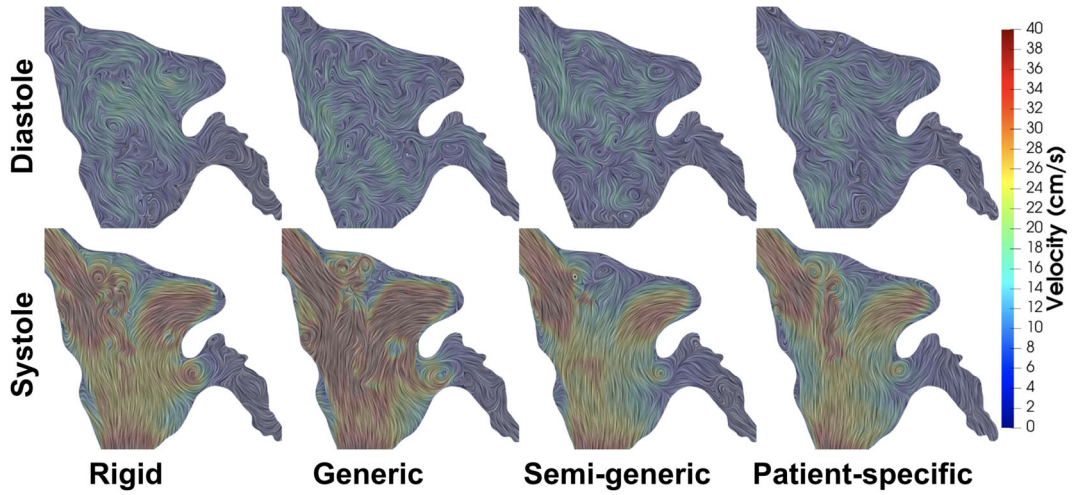

FIGURE 10 A line integral convolution of the blood flow field, colored by the velocity magnitude. The columns present the four scenarios, and the top and bottom row show vortex patterns during atrial diastole and systole, respectively.

particular, we may recognize the LA being dominated by one large vortex in the patient-specific case, and in the LAA there is a dominating vortex distal of its orifice in the rigid case, with low flow velocities below 2 cm/s toward the apex. In the generic and semi-generic cases, we observe several high-intensity vortices, with velocities up to 20 cm/s. In addition, we identify multiple recirculating regions within the LAA in the patient-specific case, notable flow traces through the orifice. The lower row of Figure 10 is captured during atrial systole, when the LA contracts and ejects blood into the left ventricle. High velocities in the cavity can be observed for all boundary condition choices, including the formation of a recirculating area in proximity of the LAA orifice. In contrast, the streamlines display apparent low-velocity vorticies trapped in the LAA in the rigid case, while the LA contraction results in an out-flux of blood in the three moving scenarios.

4 | DISCUSSION

This study examines the impact of different wall boundary conditions on local hemodynamics within the LA and LAA of a patient with permanent AF using medical imaged-based CFD. In contrast to most recent studies on LA CFD, our research focuses mainly on the numerical rather than the physiological aspect of LA modeling in patients with AF. Therefore, to assess the physiological plausibility of our results from both the rigid and moving domain simulations, we may compare them with the outcomes of previous LA CFD research.

Our results showed a number of notable differences mainly in the LAA between the different choice of boundary conditions in all hemodynamic indices, but not in the main LA cavity. Considering first the WSS, previous rigid wall studies have shown low WSS values (<0.04 Pa) in the LAA,[15,25,42,81] in agreement with our findings for the rigid wall boundary condition. Furthermore, LA studies in moving models have shown distributions of WSS comparable to us, with higher values in the LAA (<0.2 Pa).[23,30,36,46,82] Although our results are in general agreement with these previous CFD studies, one of the few direct comparisons of rigid versus moving wall boundary condition simulation studies observed an opposite trend, with higher LAA velocities and consequently higher WSS in the rigid case.[30] We may only speculate what caused this discrepancy, but geometrical factors, such as LAA length or the number of distal lobes may play an important role in local hemodynamics. For instance, the LAA in the aforementioned study was morphologically less complex than the LAA considered here, resembling a smooth thimble. Nevertheless, our measurements of WSS magnitude and distributions appear to be plausibly captured, while also confirming the large discrepancies in WSS between rigid and moving domain simulations.

Regarding OSI, previous studies using moving models have reported values between 0.25 and 0.30 in the LA cavity,[26] comparable to our observations ranging from 0.20 to 0.24. Pons et al.[35] demonstrated that patients with a history of transient ischemic attack or cerebrovascular accidents generally have higher LAA OSI. Given that the rigid case in our simulations displayed OSI values ranging between 0.1 and 0.34, in contrast to OSI values between 0.3 and 0.4 in

the moving cases, it could be suggested, based on Pons' findings, that the moving simulations might more accurately reflect the physiological condition of the present permanent AF patient. Considering RRT, previous studies have reported values of around 5 Pa^{-1} in the atrium, and maximum values ranging from 36 to 141 Pa^{-1} in AF patients.[23,46] These estimates match well with our observed RRT values between 2 and 4 Pa^{-1} in the LA cavity for all boundary conditions. The maximum values also align well with our observations in the LAA for the moving scenarios, at 53 ± 7, 16 ± 5, and 12 ± 2 Pa^{-1} in the generic, semi-generic, and patient-specific cases, respectively. However, the rigid case may overestimate RRT values in the LAA, with estimates up to 710 Pa^{-1}. Previous reports of ECAP have shown values up to 20 Pa^{-1},[36,78] while Qureshi et al.[38] proposed that ECAP values >4 Pa^{-1} indicate a high risk of thrombus formation. In this range, the generic, semi-generic, and patient-specific cases represent plausible ECAP values, with median values between 2.6 and 5.3 Pa^{-1}, while the rigid case displays median ECAP values ranging from 5 to 70 Pa^{-1}. Therefore, our spatial distribution of both RRT and ECAP is consistent with those obtained from other patient-specific studies,[35,36,78] although the difference in magnitude suggests that the rigid case may overestimate these indices.[76]

To complement the wall-measured hemodynamic indices, the KE has been considered a potential hemodynamic biomarker for thrombus formation risk.[40] Note the discrepancies in the reported KE units in various studies, including cm^2/s^2, mJ, and J/m^3. We reported the KE per mass unit, and observed consistent and high KE within the rigid LA cavity, reflective of rigid case's higher peak velocity prescribed at the PVs in comparison to the moving scenarios. Similarly, the increased cardiac output related to the generic case is reflected in the KE values, notably higher compared with the other scenarios. In contrast, there was major cycle-to-cycle variability in KE in the rigid LAA, and considerable differences in median KE values; 0.03, 1.7, 2.0, and 4.9 cm^2/s^2 in the rigid, generic, semi-generic, and patient-specific cases, respectively. In comparison to our findings in the rigid case, García-Villalba et al.[40] demonstrated that the median KE in a rigid LAA was less than 1 cm^2/s^2 in AF patients. Following studies in moving models reported median values between 1 and 10 cm^2/s^2 in the LAA.[31,40,83] In terms of space-averaged total KE our measurements in the moving scenarios ranged from 1.3 to 2.6 mJ in the LA cavity and lower values of 4.2 to 11.2 μJ in the LAA. In the LA cavity, previous numerical studies have reported measurements between 1 and 10 mJ.[27,39,46] Furthermore, total KE measurements from MRI revealed values between 0.5 and 2 mJ,[41] although this was recorded for a healthy cohort. In the LAA, Otani et al.[18] measured the space-averaged total KE, using a patient-specific LA wall motion scenario, at the μJ scale, similar to our observation. Lastly, in terms of KE per unit volume we report values of 13.6, 2.02, 1.05, and 10.3 J/m^3 for the rigid, generic, semi-generic, and patient-specific cases, respectively, which is comparable to the measurements by Dillon-Murphy et al.,[84] reporting values in the LA between 6 and 15 J/m^3. Consequently, the aforementioned computational and clinical measurements can be used to assess both the numerical and physiological accuracy of our simulations, also indicating that our reported values reside within a plausible KE regime.

Finally, we considered the velocity and flow patterns. We observed qualitatively similar velocity profiles through the LA cavity relative to the input flow rate, and noticed a large systolic vortex in the patient-specific case consistent with reported findings using MRI measurements.[6,85] In contrast, velocity profiles and flow patterns were considerably different in the LAA between the boundary conditions. First, we observed that the rigid case exhibited no oscillations across the LAA orifice—a phenomenon previously observed in LAAs of comparable complexity,[17] which may be a sign of low washout. Second, the generic case displayed only minor flow instabilities, but exhibited an increased cardiac output based off the area under the curve. Third, low velocities (<2 cm/s) observed in the rigid case appeared to give rise to patterns that resemble Moffatt eddies toward the LAA apex, a phenomenon characterized by eddies decreasing in size and intensity,[86] potentially indicating an increased risk of flow stasis toward the inner LAA lobes. However, we observed low LAA velocity peaks in all four simulations (<10 cm/s), which is in accordance with past studies reporting low velocities (<20 cm/s) inside the LAA in AF patients,[19,21,28,48,84] and acknowledged as one of the most prevalent risk factors associated with an increased likelihood of thrombus formation.[38,87] Despite similar peak LAA velocities, our observations highlight significant changes in the LAA velocity profiles and flow patterns between rigid and moving scenarios, which may have potential implications for the assessment of risk of thrombus formation in AF patients.

Generic motion models are already actively used in LA fluid simulation studies,[26,32,36] yet validation against patient-derived motion is rarely addressed. This underscores a considerable knowledge gap regarding whether generic models can serve as reliable surrogates for patient-specific motion when such data are unavailable. To address this, we analyzed two scenarios using a generic movement model, comparing them with patient-derived motion. Qualitatively, no discernible differences in hemodynamic indices were observed between the semi-generic and patient-specific cases in the LA cavity. The generic case, while matching peak velocity, showed a 30% increase in cardiac output. This led to variations in magnitude, as reflected by increased WSS and decreased RRT and ECAP in the cavity. However, all moving cases demonstrated median ECAP values below 0.5 Pa^{-1}, indicating a low risk of thrombus formation in this region.[38]

In the LAA, both the generic and semi-generic cases demonstrated similar RRT and ECAP values, highlighting the generic model's ability in predicting the risk of thrombus formation. Peak values localized at the lobes were observed in all moving scenarios, with a magnitude difference observed between the two generic cases and the patient-specific one. Nevertheless, median ECAP values across different scenarios were consistent, registering 4.2, 5.6, and 2.6 Pa^{-1} for generic, semi-generic, and patient-specific cases, respectively, aligning with the expected range of 0.1–10 Pa^{-1}.[76] These are markedly lower than the median ECAP value of 33 Pa^{-1} measured in the rigid case. This investigation suggests the generic approach's effectiveness in identifying regions at risk of thrombus formation and prolonged residence times, offering a viable alternative when patient-specific data are unavailable.

Image-based CFD studies come with a number of general limitations and potential error sources, including image segmentation and registration variability,[88,89] mitral valve modeling,[90] and non-Newtonian modeling,[91,92] which also apply to our study. Additionally, it is worth mentioning, in particular, the single-case study design, which may to some extent limit the clinical applicability and academic impact of our research. The LA geometry in our study exhibits a notably larger size, measuring approximately 128 mL at the onset of atrial diastole. This is in contrast to the normal range of 89 ± 5 mL observed in a healthy population,[41] although it is worth noting that reduced LA function is a prevalent characteristic among patients with permanent AF.[44] The larger size may potentially lead to more stable flow patterns, which could have implications for the conclusions drawn from our study as well as the resolution requirements.[42] Furthermore, we acknowledge that the patient-specific motion extracted from a single AF patient may not be representative of the typical LA motion, which could limit the general applicability of our findings. Expanding the study to a larger cohort of atrial geometries and motions is an obvious direction of future research. However, considering the challenges in acquiring time-resolved CT scans and the general scarcity of patient-specific ground truth LA motion, our research provides valuable insight into the importance of accurately capturing the LA wall motion.

Second, we acknowledge that LA wall motion in permanent AF is usually irregular and challenging to synchronize with the R–R interval based on normal sinus rhythm. However, while there is a lack of active contraction, the LA motion extracted from the medical images result in a volume change that distinctly describes the different LA functions, including the reservoir and conduit phase. This is reflected in the medical images and the resulting surface models, where we can observe a notable longitudinal displacement of the MV orifice and the passive filling of the LV.

Third, we have made a trade-off between using the same PV flow rates and having a constant cardiac output (CO). As shown in Figure 4, the PV flow rates between the rigid and patient-specific cases are noticeably different. The flow rates were derived following the principles of mass conservation according to Equation (10), thus ensuring constant CO in all scenarios. To validate this, we calculated the flow rate through the MV orifice during simulations. The resulting MV flow rate profiles are shown in Figure 11, showing negligible net flow during atrial diastole, followed by a qualitatively similar outflow during atrial systole for the rigid, semi-generic, and patient-specific cases. Furthermore, the MV flow rate values calculated from during the generic case simulation show clear resemblance to its reference curve.[19] With the exception of the generic case, the simulations displayed negligible difference in CO, with a maximum

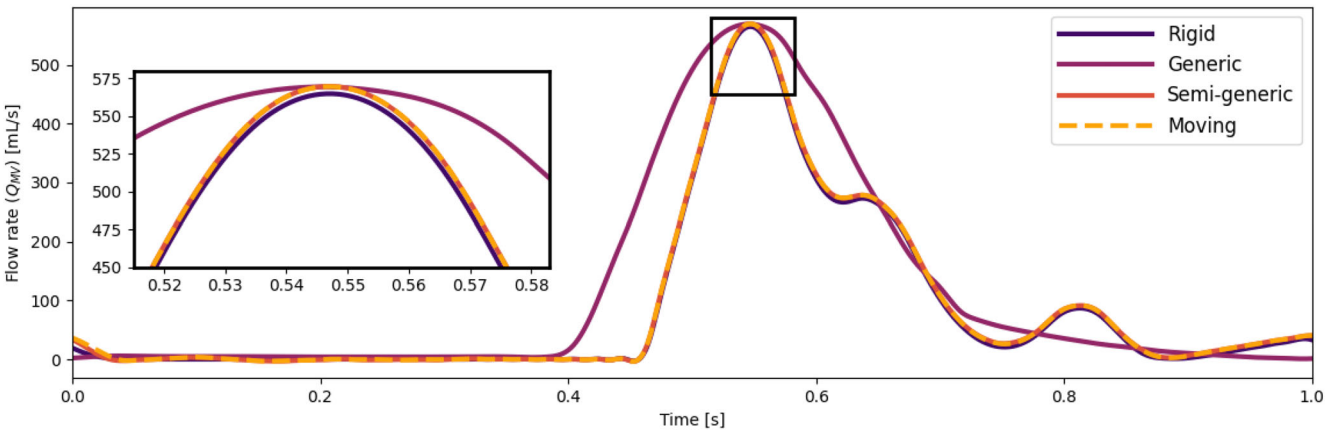

FIGURE 11 A visualization of the computed total flow rates passing through the MV orifice during the last cardiac cycle, for each of the wall boundary conditions. The flow rates were computed from the computational fluid dynamic simulation, and included a zoomed-in view of the peak flow rate during early ventricular diastole when the left ventricle relaxes.

variation of 3% in peak flow rate during early ventricular diastole, as emphasized in the zoomed-in view in Figure 11. This underscores the robustness and reliability of our computational methodology for assessing a constant CO.

Lastly, we did not have access to patient-specific flow rates or flow split. Despite PV flow rates not being patient-derived, the MV orifice's velocity curve closely resembled ultrasound measurements, showing similar maxima and a diminished A-wave, characteristic of AF patients.[93] Furthermore, the measured mean and maximum velocity magnitudes at the PVs (13 and 70 cm/s, respectively) corresponded to realistic values.[85,94] Regarding the split of the PV flow, we assumed an equal distribution of the velocity in the PVs, as opposed to an equal flow rate split that previously aligned well with MRI measurements.[95] This choice was driven by the fact that an equal flow rate split would yield similar peak velocities at the four main PVs, but would cause a five-fold larger peak velocity at the middle PV than the reported average.[96] Hence, we selected the equal velocity approach because it results in more plausible velocities and improved numerical stability.

5 | CONCLUSION

The methodological aspect of computational LA studies is still in its infancy, with a lack of knowledge on how modeling assumptions impact local hemodynamics, proposed indicators of thrombus formation and stroke, and other flow-related quantities. As a step toward addressing this challenge, our study presents a detailed methodology by providing not only complete transparency into our modeling choices and their impact but also making our morphological and computational frameworks openly accessible. A critical component of our approach is a rigorous convergence study, which we have conducted to ensure the reliability and accuracy of our computational results. Thus, our framework for LA simulations leverages medical image-based CFD, not only to study the impact of wall boundary conditions but also for high-fidelity LA CFD modeling in general.

In addition, this study contributes to the field by validation of a generic boundary condition in comparison to patient-specific data. While patient-specific data are considered the gold standard due to its capability to account for the unique anatomical characteristics of individual patients, it is laborious and time-consuming to obtain. Additionally, there are significant challenges associated with complying with protection regulations concerning data sharing, and the use of time-resolved CT scans is not commonly adopted in current clinical practice. As an alternative, generic models can provide a simplified and widely applicable representation of the LA and LAA dynamics. Although the validity of such models is often questioned due to the fact that they may not capture all the nuances of individual patient characteristics, our validation demonstrates its efficacy in replicating LA and LAA hemodynamics.

Finally, our findings also underscore the importance of incorporating moving boundary conditions in LA CFD modeling, demonstrating that the rigid wall model is not a physiologically plausible assumption by potentially overestimating proposed predictors of thrombus formation. We reveal that even in later stages of AF, a degree of passive atrial contraction significantly contributes to complex flow patterns in the LA and more efficient blood washout in the LAA.

AUTHOR CONTRIBUTIONS

H. A. Kjeldsberg was responsible for the research, and writing of the paper as well as software implementation. D. V. Medel provided the medical image and Doppler echocardiography recordings of the mitral valve used for velocity profile validation. C. Albors, J. Mill, and O. Camara performed image segmentation and registration, and provided the corresponding surface models. K. Valen-Sendstad and J. Sundnes provided valuable assistance in planning, reviewing, shaping, and improving the quality of the final manuscript. All authors read and approved the final manuscript.

ACKNOWLEDGMENTS

This research was funded, in whole or in part, by The Research Council of Norway through the PARIS project (311117) and by ERACoSysMed under grant agreement no. 643271. We also acknowledge funding by the SimCardioTest project (Digital transformation in Health and Care SC1-DTH-06-2020) under grant agreement no. 101016496. Simulations were performed on the Saga cluster, with resources provided by UNINETT Sigma2—the National Infrastructure for High Performance Computing and Data Storage in Norway, grant number nn9249k, and on the Oracle HPC Cluster stack through Oracle Cloud credits and related resources provided by Oracle for Research.

CONFLICT OF INTEREST STATEMENT

The authors declare no conflicts of interest.

DATA AVAILABILITY STATEMENT

The dataset analyzed for this study can be obtained from the authors on reasonable request. The software related to the CFD simulation can be located online at https://github.com/KVSlab/OasisMove. The software used for the preprocessing and postprocessing can be found online at https://github.com/KVSlab/VaMPy.

ORCID

Kristian Valen-Sendstad https://orcid.org/0000-0002-2907-0171

REFERENCES

1. Wolf PA, Abbott RD, Kannel WB. Atrial fibrillation as an independent risk factor for stroke: the Framingham study. *Stroke*. 1991;22(8):983-988. doi:10.1161/01.STR.22.8.983
2. Thijssen VL, Ausma J, Borgers M. Structural remodelling during chronic atrial fibrillation: act of programmed cell survival. *Cardiovasc Res*. 2001;52(1):14-24. doi:10.1016/S0008-6363(01)00367-4
3. Polyakova V, Miyagawa S, Szalay Z, Risteli J, Kostin S. Atrial extracellular matrix remodelling in patients with atrial fibrillation. *J Cell Mol Med*. 2008;12(1):189-208. doi:10.1111/j.1582-4934.2008.00219.x
4. Cresti A, García-Fernández MA, Sievert H, et al. Prevalence of extra-appendage thrombosis in non-valvular atrial fibrillation and atrial flutter in patients undergoing cardioversion: a large transoesophageal echo study. *EuroIntervention*. 2019;15(3):e225-e230.
5. Ding WY, Gupta D, Lip GY. Atrial fibrillation and the prothrombotic state: revisiting Virchow's triad in 2020. *Heart*. 2020;106(19):1463-1468. doi:10.1136/heartjnl-2020-316977
6. Fyrenius A, Wigström L, Ebbers T, Karlsson M, Engvall J, Bolger AF. Three dimensional flow in the human left atrium. *Heart*. 2001;86(4):448-455. doi:10.1136/heart.86.4.448
7. Fluckiger JU, Goldberger JJ, Lee DC, et al. Left atrial flow velocity distribution and flow coherence using four-dimensional FLOW MRI: a pilot study investigating the impact of age and pre-and postintervention atrial fibrillation on atrial hemodynamics. *J Magn Reson Imaging*. 2013;38(3):580-587. doi:10.1002/jmri.23994
8. Markl M, Fluckiger J, Lee DC, Ng J, Goldberger JJ. Velocity quantification by electrocardiography-gated phase contrast magnetic resonance imaging in patients with cardiac arrhythmia: a simulation study based on real time transesophageal echocardiography data in atrial fibrillation. *J Comput Assist Tomogr*. 2015;39(3):422-427. doi:10.1097/RCT.0000000000000207
9. Pollick C, Taylor D. Assessment of left atrial appendage function by transesophageal echocardiography. Implications for the development of thrombus. *Circulation*. 1991;84(1):223-231. doi:10.1161/01.CIR.84.1.223
10. Nakai H, Takeuchi M, Nishikage T, Nagakura T, Otani S. The mitral L wave. *Circ J*. 2007;71(8):1244-1249. doi:10.1253/circj.71.1244
11. Park KH, Son JW, Park WJ, et al. Characterization of the left atrial vortex flow by two-dimensional transesophageal contrast echocardiography using particle image velocimetry. *Ultrasound Med Biol*. 2013;39(1):62-71. doi:10.1016/j.ultrasmedbio.2012.08.013
12. Dahl SK, Thomassen E, Hellevik LR, Skallerud B. Impact of pulmonary venous locations on the intra-atrial flow and the mitral valve plane velocity profile. *Cardiovasc Eng Technol*. 2012;3:269-281. doi:10.1007/s13239-012-0099-1
13. García-Isla G, Olivares AL, Silva E, et al. Sensitivity analysis of geometrical parameters to study haemodynamics and thrombus formation in the left atrial appendage. *Int J Numer Method Biomed Eng*. 2018;34(8):e3100. doi:10.1002/cnm.3100
14. Mill J, Harrison J, Legghe B, et al. In-silico analysis of the influence of pulmonary vein configuration on left atrial haemodynamics and thrombus formation in a large cohort. In: Ennis DB, Perotti LE, Wang VY, eds. *Functional Imaging and Modeling of the Heart. FIMH 2021. Lecture Notes in Computer Science*. Vol 12738. 1st ed. Springer; 2021:605-616.
15. Dueñas-Pamplona J, Garcia JG, Castro F, Muñoz-Paniagua J, Goicolea J, Pallares JS. Morphing the left atrium geometry: a deeper insight into blood stasis within the left atrial appendage. *App Math Model*. 2022;108:27-45. doi:10.1016/j.apm.2022.03.012
16. Sanatkhani S, Nedios S, Menon PG, Bollmann A, Hindricks G, Shroff SG. Subject-specific calculation of left atrial appendage blood-borne particle residence time distribution in atrial fibrillation. *Front Physiol*. 2021;12:633135.
17. Alinezhad L, Ghalichi F, Ahmadlouydarab M, Chenaghlou M. Left atrial appendage shape impacts on the left atrial flow hemodynamics: a numerical hypothesis generating study on two cases. *Comput Methods Programs Biomed*. 2022;213:106506.
18. Otani T, Al-Issa A, Pourmorteza A, McVeigh ER, Wada S, Ashikaga H. A computational framework for personalized blood flow analysis in the human left atrium. *Ann Biomed Eng*. 2016;44(11):3284-3294. doi:10.1007/s10439-016-1590-x
19. Bosi GM, Cook A, Rai R, et al. Computational fluid dynamic analysis of the left atrial appendage to predict thrombosis risk. *Front Cardiovasc Med*. 2018;5:34.
20. Masci A, Barone L, Dedè L, et al. The impact of left atrium appendage morphology on stroke risk assessment in atrial fibrillation: a computational fluid dynamics study. *Front Physiol*. 2019;9:1938.
21. Fanni BM, Capellini K, di Leonardo M, et al. Correlation between LAA morphological features and computational fluid dynamics analysis for non-valvular atrial fibrillation patients. *Appl Sci*. 2020;10(4):1448. doi:10.3390/app10041448
22. Zhang LT, Gay M. Characterizing left atrial appendage functions in sinus rhythm and atrial fibrillation using computational models. *J Biomech*. 2008;41(11):2515-2523. doi:10.1016/j.jbiomech.2008.05.012

23. Koizumi R, Funamoto K, Hayase T, et al. Numerical analysis of hemodynamic changes in the left atrium due to atrial fibrillation. *J Biomech*. 2015;48(3):472-478. doi:10.1016/j.jbiomech.2014.12.025
24. Masci A, Alessandrini M, Forti D, et al. A proof of concept for computational fluid dynamic analysis of the left atrium in atrial fibrillation on a patient-specific basis. *J Biomech Eng*. 2020;142(1):011002.
25. Wang Y, Qiao Y, Mao Y, Jiang CY, Fan JR, Luo K. Numerical prediction of thrombosis risk in left atrium under atrial fibrillation. *Math Biosci Eng*. 2020;17(3):2348-2360. doi:10.3934/mbe.2020125
26. Paliwal N, Ali RL, Salvador M, et al. Presence of left atrial fibrosis may contribute to aberrant hemodynamics and increased risk of stroke in atrial fibrillation patients. *Front Physiol*. 2021;12:657452.
27. Otani T, Yoshida T, Yi W, Endo S, Wada S. On the impact of left upper lobectomy on the left atrial hemodynamics. *Front Physiol*. 2022;13:830436.
28. Jia D, Jeon B, Park HB, Chang HJ, Zhang LT. Image-based flow simulations of pre-and post-left atrial appendage closure in the left atrium. *Cardiovasc Eng Technol*. 2019;10(2):225-241. doi:10.1007/s13239-019-00412-7
29. Mill J, Agudelo V, Li CH, et al. Patient-specific flow simulation analysis to predict device-related thrombosis in left atrial appendage occluders. *Interv Cardiol*. 2021;3(4):278-285.
30. Dueñas-Pamplona J, García JG, Sierra-Pallares J, Ferrera C, Agujetas R, López-Mínguez JR. A comprehensive comparison of various patient-specific CFD models of the left atrium for atrial fibrillation patients. *Comput Biol Med*. 2021;133:104423. doi:10.1016/j.compbiomed.2021.104423
31. Gonzalo A, García-Villalba M, Rossini L, et al. Non-Newtonian blood rheology impacts left atrial stasis in patient-specific simulations. *Int J Numer Method Biomed Eng*. 2022;38(6):e3597. doi:10.1002/cnm.3597
32. Mill J, Agudelo V, Olivares AL, et al. Sensitivity analysis of in silico fluid simulations to predict thrombus formation after left atrial appendage occlusion. *Mathematics*. 2021;9(18):2304. doi:10.3390/math9182304
33. Malek AM, Alper SL, Izumo S. Hemodynamic shear stress and its role in atherosclerosis. *JAMA*. 1999;282(21):2035-2042.
34. Samady H, Eshtehardi P, McDaniel MC, et al. Coronary artery wall shear stress is associated with progression and transformation of atherosclerotic plaque and arterial remodeling in patients with coronary artery disease. *Circulation*. 2011;124(7):779-788. doi:10.1161/CIRCULATIONAHA.111.021824
35. Pons MI, Mill J, Fernandez-Quilez A, et al. Joint analysis of morphological parameters and in silico haemodynamics of the left atrial appendage for thrombogenic risk assessment. *J Interv Cardiol*. 2022;2022:1-10. doi:10.1155/2022/9125224
36. Corti M, Zingaro A, Dedé L, Quarteroni AM. Impact of atrial fibrillation on left atrium haemodynamics: a computational fluid dynamics study. *Comput Biol Med*. 2022;150:106143.
37. Aguado AM, Olivares AL, Yagüe C, et al. In silico optimization of left atrial appendage occluder implantation using interactive and modeling tools. *Front Physiol*. 2019;10:237.
38. Qureshi A, Balmus M, Williams SE, et al. Modelling virchow's triad to improve stroke risk assessment in atrial fibrillation patients. *Computing in Cardiology*. IEEE; 2022:1-4. doi:10.3389/fphys.2019.00237
39. Feng L, Gao H, Griffith B, Niederer S, Luo X. Analysis of a coupled fluid-structure interaction model of the left atrium and mitral valve. *Int J Numer Method Biomed Eng*. 2019;35(11):e3254. doi:10.1002/cnm.3254
40. García-Villalba M, Rossini L, Gonzalo A, et al. Demonstration of patient-specific simulations to assess left atrial appendage thrombogenesis risk. *Front Physiol*. 2021;12:596596. doi:10.3389/fphys.2021.596596
41. Arvidsson PM, Töger J, Heiberg E, Carlsson M, Arheden H. Quantification of left and right atrial kinetic energy using four-dimensional intracardiac magnetic resonance imaging flow measurements. *J Appl Physiol*. 2013;114(10):1472-1481. doi:10.1152/japplphysiol.00932.2012
42. Khalili E, Daversin-Catty C, Olivares AL, Mill J, Camara O, Valen-Sendstad K. On the importance of fundamental computational fluid dynamics toward a robust and reliable model of left atrial flows. *Int J Numer Method Biomed Eng*. 2024;40:e3804. doi:10.1002/cnm.3804
43. Thomas L, Levett K, Boyd A, Leung DYC, Schiller NB, Ross DL. Compensatory changes in atrial volumes with normal aging: is atrial enlargement inevitable? *J Am Coll Cardiol*. 2002;40(9):1630-1635. doi:10.1016/S0735-1097(02)02371-9
44. Habibi M, Lima JA, Khurram IM, et al. Association of left atrial function and left atrial enhancement in patients with atrial fibrillation: cardiac magnetic resonance study. *Circ Cardiovasc Imaging*. 2015;8(2):e002769. doi:10.1161/CIRCIMAGING.114.002769
45. Njoku A, Kannabhiran M, Arora R, et al. Left atrial volume predicts atrial fibrillation recurrence after radiofrequency ablation: a meta-analysis. *Europace*. 2018;20(1):33-42. doi:10.1093/europace/eux013
46. Zingaro A, Dedè L, Menghini F, Quarteroni A. Hemodynamics of the heart's left atrium based on a variational multiscale-LES numerical method. *Eur J Mech B Fluids*. 2021;89:380-400. doi:10.1016/j.euromechflu.2021.06.014
47. D'Alessandro N, Masci A, Andalò A, et al. Simulation of the hemodynamic effects of the left atrial appendage occlusion in atrial fibrillation: preliminary results. *Proceedings of the Computing in Cardiology*. IEEE; 2020:1-4.
48. Fang R, Wang Z, Zhao X, et al. Stroke risk evaluation for patients with atrial fibrillation: insights from left atrial appendage with fluid-structure interaction analysis. *Comput Biol Med*. 2022;148:105897.
49. Musotto G, Monteleone A, Vella D, et al. The role of patient-specific morphological features of the left atrial appendage on the thromboembolic risk under atrial fibrillation. *Front Cardiovasc Med*. 2022;9:894187. doi:10.3389/fcvm.2022.894187
50. Avants BB, Tustison N, Song G. Advanced normalization tools (ANTS). *Insight J*. 2009;2(365):1-35.
51. Pieper S, Halle M, Kikinis R. *3D Slicer*. 1st ed. IEEE; 2004:632-635.

52. Schmidt R, Singh K. meshmixer: an interface for rapid mesh composition. *SIGGRAPH'10. International Conference on Computer Graphics and Interactive Techniques*. Association for Computing Machinery; 2010.
53. Kjeldsberg HA, Bergersen AW, Valen-Sendstad K. VaMPy: an automated and objective pipeline for modeling vascular geometries. *J Open Source Softw*. 2023;8(85):5278. doi:10.21105/joss.05278
54. Gan L, Yu L, Xie M, Feng W, Yin J. Analysis of real-time three dimensional transesophageal echocardiography in the assessment of left atrial appendage function in patients with atrial fibrillation. *Exp Ther Med*. 2016;12(5):3323-3327. doi:10.3892/etm.2016.3745
55. Jones C, Song G, Gibson D. An echocardiographic assessment of atrial mechanical behaviour. *Heart*. 1991;65(1):31-36. doi:10.1136/hrt.65.1.31
56. Veronesi F, Corsi C, Sugeng L, et al. Quantification of mitral apparatus dynamics in functional and ischemic mitral regurgitation using real-time 3-dimensional echocardiography. *J Am Soc Echocardiogr*. 2008;21(4):347-354. doi:10.1016/j.echo.2007.06.017
57. Bonito A, Demlow A, Nochetto RH. Finite element methods for the Laplace–Beltrami operator. *Handbook of Numerical Analysis*. Elsevier; 2020:1-103.
58. Kundu P, Cohen I, Dowling D. *Fluid Mechanics*. 6th ed. Academic Press; 2015.
59. Mojica-Pisciotti ML, Panovský R, Masárová L, et al. Left atrium phasic impairments in paroxysmal atrial fibrillation patients assessed by cardiovascular magnetic resonance feature tracking. *Sci Rep*. 2022;12(1):7539.
60. Jasak H, Tukovic Z. Automatic mesh motion for the unstructured finite volume method. *Trans FAMENA*. 2006;30(2):1-20.
61. Kjeldsberg HA, Sundnes J, Valen-Sendstad K. A verified and validated moving domain computational fluid dynamics solver with applications to cardiovascular flows. *Int J Numer Method Biomed Eng*. 2023;39:e3703. doi:10.1002/cnm.3703
62. Mortensen M, Valen-Sendstad K. Oasis: a high-level/high-performance open source Navier–Stokes solver. *Comput Phys Commun*. 2015;188:177-188. doi:10.1016/j.cpc.2014.10.026
63. Khan M, Valen-Sendstad K, Steinman D. Direct numerical simulation of laminar-turbulent transition in a non-axisymmetric stenosis model for Newtonian vs. shear-thinning non-Newtonian rheologies. *Flow Turbul Combust*. 2019;102:43-72. doi:10.1007/s10494-018-9905-7
64. Bergersen AW, Mortensen M, Valen-Sendstad K. The FDA nozzle benchmark: "in theory there is no difference between theory and practice, but in practice there is". *Int J Numer Method Biomed Eng*. 2019;35(1):e3150. doi:10.1002/cnm.3150
65. Chnafa C, Brina O, Pereira V, Steinman DA. Better than nothing: a rational approach for minimizing the impact of outflow strategy on cerebrovascular simulations. *Am J Neuroradiol*. 2018;39(2):337-343. doi:10.3174/ajnr.A5484
66. Arzani A. Accounting for residence-time in blood rheology models: do we really need non-Newtonian blood flow modelling in large arteries? *J R Soc Interface*. 2018;15(146):20180486.
67. Khan MO, Arana VT, Rubbert C, et al. Association between aneurysm hemodynamics and wall enhancement on 3D vessel wall MRI. *J Neurosurg*. 2020;134(2):565-575.
68. Mancini V, Bergersen AW, Vierendeels J, Segers P, Valen-Sendstad K. High-frequency fluctuations in post-stenotic patient specific carotid stenosis fluid dynamics: a computational fluid dynamics strategy study. *Cardiovasc Eng Technol*. 2019;10:277-298. doi:10.1007/s13239-019-00410-9
69. Meschi SS, Farghadan A, Arzani A. Flow topology and targeted drug delivery in cardiovascular disease. *J Biomech*. 2021;119:110307. doi:10.1016/j.jbiomech.2021.110307
70. Karniadakis G, Sherwin SJ. *Spectral/hp Element Methods for Computational Fluid Dynamics*. 3rd ed. Oxford University Press; 2005.
71. Bazilevs Y, Gohean J, Hughes T, Moser RD, Zhang Y. Patient-specific isogeometric fluid–structure interaction analysis of thoracic aortic blood flow due to implantation of the Jarvik 2000 left ventricular assist device. *Comput Methods Appl Mech Eng*. 2009;198(45–46):3534-3550.
72. D'Alessandro N, Falanga M, Masci A, Severi S, Corsi C. Preliminary findings on left atrial appendage occlusion simulations applying different endocardial devices. *Front Cardiovasc Med*. 2023;10:220.
73. Casa LD, Deaton DH, Ku DN. Role of high shear rate in thrombosis. *J Vasc Surg*. 2015;61(4):1068-1080. doi:10.1016/j.jvs.2014.12.050
74. Ku DN, Giddens DP, Zarins CK, Glagov S. Pulsatile flow and atherosclerosis in the human carotid bifurcation. Positive correlation between plaque location and low oscillating shear stress. *Arteriosclerosis*. 1985;5(3):293-302. doi:10.1161/01.ATV.5.3.293
75. Sugiyama S, Niizuma K, Nakayama T, et al. Relative residence time prolongation in intracranial aneurysms: a possible association with atherosclerosis. *Neurosurgery*. 2013;73(5):767-776. doi:10.1227/NEU.0000000000000096
76. di Achille P, Tellides G, Figueroa C, Humphrey JD. A haemodynamic predictor of intraluminal thrombus formation in abdominal aortic aneurysms. *Proc R Soc A: Math Phys Eng Sci*. 2014;470(2172):20140163. doi:10.1098/rspa.2014.0163
77. Gorring N, Kark L, Simmons A, Barber T. Determining possible thrombus sites in an extracorporeal device, using computational fluid dynamics-derived relative residence time. *Comput Methods Biomech Biomed Eng*. 2015;18(6):628-634.
78. Morales X, Mill J, Juhl KA, et al. Deep learning surrogate of computational fluid dynamics for thrombus formation risk in the left atrial appendage. In: Pop M, Sermesant M, Camara O, et al., eds. *Statistical Atlases and Computational Models of the Heart. Multi-Sequence CMR Segmentation, CRT-EPiggy and LV Full Quantification Challenges. STACOM 2019. Lecture Notes in Computer Science*. Vol 12009. 1st ed. Springer; 2020:157-166.
79. Kjeldsberg HA, Bergersen AW, Valen-Sendstad K. morphMan: automated manipulation of vascular geometries. *J Open Source Softw*. 2019;4(35):1065. doi:10.21105/joss.01065
80. Luciano RD, Chen X, Bergstrom DJ. Turbulence in simulations of blood flow in cerebral arteries with aneurysms. *Proceedings of the 12th International Symposium on Turbulence and Shear Flow Phenomena*. TSFP; 2022.

81. Grigoriadis GI, Sakellarios AI, Kosmidou I, et al. Wall shear stress alterations at left atrium and left atrial appendage employing abnormal blood velocity profiles. *42nd Annual International Conference of the IEEE Engineering in Medicine & Biology Society (EMBC)*. IEEE; 2020:2565-2568.
82. Lameu J, Sandoval I, Salinet J. Thrombogenesis and hemodynamics in left atrium under atrial fibrillation. *Computing in Cardiology*. IEEE; 2022:1-4.
83. Durán E, García-Villalba M, Martínez-Legazpi P, et al. Pulmonary vein flow split effects in patient-specific simulations of left atrial flow. *Comput Biol Med*. 2023;163:107128. doi:10.1016/j.compbiomed.2023.107128
84. Dillon-Murphy D, Marlevi D, Ruijsink B, et al. Modeling left atrial flow, energy, blood heating distribution in response to catheter ablation therapy. *Front Physiol*. 2018;9:1757.
85. Garcia J, Sheitt H, Bristow MS, et al. Left atrial vortex size and velocity distributions by 4D flow MRI in patients with paroxysmal atrial fibrillation: associations with age and CHA_2DS_2-VASc risk score. *J Magn Reson Imaging*. 2020;51(3):871-884. doi:10.1002/jmri.26876
86. Moffatt HK. Viscous and resistive eddies near a sharp corner. *J Fluid Mech*. 1964;18(1):1-18. doi:10.1017/S0022112064000015
87. Takada T, Yasaka M, Nagatsuka K, Minematsu K, Yamaguchi T. Blood flow in the left atrial appendage and embolic stroke in nonvalvular atrial fibrillation. *Eur Neurol*. 2001;46(3):148-152. doi:10.1159/000050788
88. Valen-Sendstad K, Bergersen AW, Shimogonya Y, et al. Real-world variability in the prediction of intracranial aneurysm wall shear stress: the 2015 international aneurysm CFD challenge. *Cardiovasc Eng Technol*. 2018;9(4):544-564. doi:10.1007/s13239-018-00374-2
89. Steinman DA, Pereira VM. How patient specific are patient-specific computational models of cerebral aneurysms? An overview of sources of error and variability. *Neurosurg Focus*. 2019;47(1):E14. doi:10.3171/2019.4.FOCUS19123
90. Vedula V. *Image Based Computational Modeling of Intracardiac Flows*. PhD thesis. Johns Hopkins University; 2015.
91. Long Q, Merrifield R, Xu X, Kilner P, Firmin DN, Yang GZ. Subject-specific computational simulation of left ventricular flow based on magnetic resonance imaging. *Proc Inst Mech Eng H: J Eng Med*. 2008;222(4):475-485. doi:10.1243/09544119JEIM310
92. Lantz J, Gupta V, Henriksson L, et al. Intracardiac flow at 4D CT: comparison with 4D flow MRI. *Radiology*. 2018;289(1):51-58. doi:10.1148/radiol.2018173017
93. Albors C, Mill J, Kjeldsberg HA, et al. Sensitivity analysis of left atrial wall modeling approaches and inlet/outlet boundary conditions in fluid simulations to predict thrombus formation. In: Camara O, Puyol-Antón E, Qin C, et al., eds. *Statistical Atlases and Computational Models of the Heart. Regular and CMRxMotion Challenge Papers*. Springer; 2023:179-189.
94. Markl M, Carr M, Ng J, et al. Assessment of left and right atrial 3D hemodynamics in patients with atrial fibrillation: a 4D flow MRI study. *Int J Cardiovasc Imaging*. 2016;32:807-815. doi:10.1007/s10554-015-0830-8
95. Lantz J, Gupta V, Henriksson L, et al. Impact of pulmonary venous inflow on cardiac flow simulations: comparison with in vivo 4D flow MRI. *Ann Biomed Eng*. 2019;47(2):413-424. doi:10.1007/s10439-018-02153-5
96. Nishimura RA, Abel MD, Hatle LK, Tajik AJ. Relation of pulmonary vein to mitral flow velocities by transesophageal Doppler echocardiography. Effect of different loading conditions. *Circulation*. 1990;81(5):1488-1497.

SUPPORTING INFORMATION

Additional supporting information can be found online in the Supporting Information section at the end of this article.

How to cite this article: Kjeldsberg HA, Albors C, Mill J, et al. Impact of left atrial wall motion assumptions in fluid simulations on proposed predictors of thrombus formation. *Int J Numer Meth Biomed Engng*. 2024;40(6): e3825. doi:10.1002/cnm.3825